

Computationally designed ssDNA modular nanorobots for cancer recognition, toehold disintegration, visual diagnosis and synergistic gene silencing

Xiaotong Shen

Beijing Normal University

Qingwen Ouyang

Beijing Normal University

Hongwei Tan

Beijing Normal University

Jin Ouyang

Beijing Normal University

Na Na (✉ nana@bnu.edu.cn)

Beijing Normal University <https://orcid.org/0000-0002-0474-8409>

Article

Keywords: single-stranded DNA modular nanorobots, computational design, toehold disintegration, visual dual diagnosis, synergistic gene silencing

Posted Date: February 1st, 2022

DOI: <https://doi.org/10.21203/rs.3.rs-1026581/v1>

License:  This work is licensed under a Creative Commons Attribution 4.0 International License.

[Read Full License](#)

Abstract

Single-stranded DNA (ssDNA) allows more flexible and directional modifications than relatively rigid double-stranded DNA (dsDNA) in a 'side-by-side' manner. However, ssDNA applications are greatly limited by their poor stability from the 'atom equivalents' design, suffering from increased folding errors and complicated sequence optimizations. Herein, via all-atom molecular dynamics (MD) simulations, a molecular dynamics simulation of the dynamic folding of ssDNA in the self-assembly process was examined and optimized. This guided the intelligent construction of a stable frame structure of tetrahedral ssDNA modular nanorobots, which are convenient for diagnosis and therapy applications. The ssDNA modular nanorobots were assembled with five functional modules, which included tetrahedron skeleton fixation, tumour cell membrane protein dual recognition, enzyme loading, dual-targeted miRNA detection and synergy siRNA loading. As demonstrated, the ssDNA modular nanorobots were stable, flexible, and highly utilized, and had low folding errors. For intracellular delivery, a two-apptamer logic gate was constructed for tumour cell membrane protein dual recognition, obtaining efficient and cancer-selective internalization of ssDNA nanorobots with reagent loading. Then, in cancer cells with high expression of target miRNAs (miR-21 and miR-224), toehold disintegration was initiated by two RCA reactions for precise and visualized dual detection. Simultaneously, the released disintegrated modules triggered synergistic gene silencing by two loaded siRNAs, which resulted in a 95.6% cure rate in 17 days. This work has provided a computationally designed pathway for constructing flexible ssDNA modular nanorobots, showing better multiflexibility and applicability than relatively rigid dsDNA nanostructures.

Introduction

With the development of DNA nanomaterials, DNA nanorobots have exhibited great potential for intelligent drug delivery based on responses to molecular triggers¹. To guarantee molecular robots with toehold motions in bionic systems, the design of base sequences and configurations is highly rigorous for constructing sophisticated DNA nanostructures². As a breakthrough in nanotechnology, DNA origami enables rationale and flexible design to obtain three-dimensional (3D) DNA nanostructures with controlled sizes, varied shapes and spatial addressabilities³⁻⁵. Nevertheless, the current applications of DNA nanostructures are mainly concentrated on the configuration of double-stranded DNA (dsDNA) structures. With double-stranded structures in a 'side-by-side' manner, the relatively rigid dsDNA has relatively poor modifiability, low base utilization and inefficient toehold dynamics. To some extent, these have become major limitations of the biological applications of DNA nanostructures⁶. By comparison, without covalent double chains, single-stranded DNA (ssDNA) allows facile self-assembly of nanostructures with low valence and directional bonding^{7,8}. This endows ssDNAs with better flexibility of modifications compared with the 'side-by-side' manner of rigid dsDNA. However, with atomic- or biomacromolecule-like interactions, ssDNAs designed in 'atom equivalents' suffer from poor stability, increased folding errors and complicated sequence optimizations. These characteristics greatly challenge

the design and optimization of ssDNA sequences to fold 3D origami with special functions, which hinders further reliable bioapplications.

Meanwhile, computational calculations have been introduced into traditional dsDNA origami to fabricate stable strands and obtain rigid 3D structures^{9,10}. Currently, all-atom molecular dynamics (MD) simulations can be applied to characterize the structural and mechanical properties of dsDNAs in unprecedented microscopic detail¹¹. In an automated manner, MD simulations allowed rapid multicomponent assemblies with fine control over the geometrical, mechanical and dynamical properties of DNA 3D structures¹². Although computational calculations have not been reported for ssDNA design, they would be expected to show great potential for designing ssDNA nanostructures. Therefore, to accelerate *in vivo* multiapplications of ssDNA modular nanorobots, computational simulation of dynamic folding of ssDNA in all-atom modelling could make great contributions.

Herein, based on MD simulations, a ssDNA modular nanorobot with a tetrahedral skeleton was designed. By examining the dynamic folding of the ssDNA self-assembly in all-atom modelling, MD was devoted to optimizing and constructing stable frame structures. Therefore, a ssDNA modular nanorobot with multifunctional modules was successfully designed with high base utilization, multifunctionality and low folding errors. The ssDNA modular nanorobot consisted of five modules, all of which were applied to their functions. Therefore, multiple functions, including logic cell recognition, endosomal escape, toehold self-disintegration, visualized dual diagnosis and synergistic gene silencing, were successfully realized *in vivo*. This smart computational design ensured the stable and efficient multifunctions of the ssDNA modular nanorobots. It was crucial to provide a comprehensive and efficient strategy for cancer recognition, toehold disintegration, visual dual diagnosis and synergistic gene silencing.

Results And Discussion

Design and computational simulation of ssDNA modular nanorobots.

The ssDNA modular nanorobot was designed by the Watson-Crick base-pairing principle¹³. To obtain high base utilization, the design was guided and optimized by MD simulation of the dynamic folding process in all-atom modelling. As designed, nucleic acids were self-assembled to fabricate frame structures with sufficient toeholds for multifunctional applications. The ssDNA modular nanorobot was proposed to contain five functional modules. As shown in Figure 1a, the functions of the five modules included tetrahedron skeleton fixation (I), logic cell membrane protein dual-recognition (II), enzyme loading (III), dual-targeted miRNA detection (IV) and synergy siRNA loading (V). To assemble the five modules into the stable frames, two main ssDNAs of D1 and D2 were designed computationally. The middle domains complemented each other to obtain the tetrahedron skeleton fixation module (I) (in red). In addition, the two ends of D1 and D2 were ligated by splint R ligases to form two closed ssDNAs (BPAB formed by D1 and CPAC formed by D2, Fig. 1a).

Meanwhile, two aptamers of sgc8c and sgc4f were designed in the middle of D1 and D2, which functionalized it as a logic cell membrane protein dual-recognition module (II) (in purple). Subsequently, phi29 DNA polymerase was loaded onto the green region to achieve enzyme loading (III) through the classic SMCC strategy^{14,15} by hybridization with enzyme-modified short ssDNAs. It should be noted that the apex angles of B and C were designed as modules for dual-targeted miRNA detection (IV). Furthermore, two siRNAs of human epidermal growth factor receptor 2 (HER2) and vascular endothelial growth factor (VEGF), reported to possess synergistic silencing roles on VEGF^{16,17}, were loaded onto the ssDNA modular nanorobot. As shown in Fig. 1a, the two siRNAs (S1: siRNAs-siVEGF, S2: siHER2) were coupled to strands of PB, PC and AB, AC to achieve synergy siRNA loading (V). It should be noted that S1 and S2 not only immobilized the tetrahedral structure but also acted as synergistic silencing reagents for cancer treatments.

During computational modelling and simulations, the dynamic folding of DNA structures was studied to guide nanorobot designs and optimizations. A biomolecular simulation program of Amber14 Software¹⁸ was adopted to examine the stability and practicability of the ssDNA modular nanorobot. As a result, the simulation of the 3D tetrahedral structure and MD in all-atom modelling with 14,880 atoms was accomplished. Characterization of the microscopic details was achieved by tracking the trajectories of all atoms of the ssDNA and the surrounding solution. For MD simulations, the overall shape of the ssDNA modular nanorobot was constructed by Gauss View 5.0 Software. After optimization, the obtained tetrahedral structures remained mostly stable and exhibited no significant structural difference between the beginning (0 ns, Fig. 1b) and the end of the MD simulations (15 ns, Fig. 1b). Simultaneously, the MD simulations were evaluated by the root-mean-square deviation (RMSD) of the DNA atoms from their initial coordinates. As shown in Fig. 1c-i, an equilibrium conformation at the end of the production run was demonstrated with relatively stable RMSD values.

The stabilization of the tetrahedron skeleton (I, Fig. 1a, 33 bases, 53-85 position) was further examined via fractions of broken base pairs between N1 of the purine base and N3 of the pyrimidine base. Initially, ~6% of the two terminal bases in the system were broken (Fig. 1c-ii), which was generated from their dynamic equilibrium process to find stable configurations. In the subsequent 4 ns, other fractions remained stable with 3% broken pairs and this even decreased to 0% after 4 ns. This confirmed the successful formation of duplex DNAs to fix the tetrahedron skeleton for Module I. The corresponding base distance changes are shown in Fig. S1.

The small fluctuation of each base in Module I was further examined by evaluating the last 10 ns of trajectories. The root-mean-square fluctuation (RMSF) values for the centre mass of the DNA base pairs were calculated for the examinations. As demonstrated (Fig. 1c-iii), most RMSF values were less than 4 Å, reaching the stable range of ssDNA bases. A relatively higher RMSF of approximately 5 Å for the terminal base pairs activated the terminal base pairs for multiple biological modifications^{19,20}. A heatmap of the fraction of broken base pairs versus the simulation time is shown in Fig. S2. Furthermore, the ssDNA modular nanorobot was also evaluated by calculating inflection points via a nucleotide-level coarse-

grained model of oxDNA²¹. After running for 2 million frames, the long ssDNA chain changed and exhibited obvious inflection points at base positions of 52 and 85 for D1 and 82 and 115 for D2. Satisfactorily, these positions were in accordance with the structural design and experimental data (Fig. S3). Therefore, by clearing the folding principle of ssDNA with computational simulations, the ssDNA modular nanorobot was designed to be stable and versatile.

Designed strategies for *in vivo* diagnosis and treatments

Scheme 1 illustrates the designed processes for cancer recognition, toehold disintegration, visualized dual-diagnosis and synergistic gene silencing treatments. Human acute lymphoblastic leukaemia cells (CEMs) were selected as models for the experiments. To ensure the aptamer-based logic recognition of CEM cells, two aptamers of sgc8c and sgc4f (overexpressed on the CEM cell membrane)^{22,23} were designed in the middle of the D1 and D2 strands. Based on logic dual recognition by two aptamers, ssDNA nanorobots target the corresponding receptors on the surfaces of tumour cells to form two G-quadruplexes. The 'locked-open' status of tumour cell logic recognition was controlled by this specific dual recognition (Scheme 1-a). Subsequently, the ssDNA modular nanorobots were internalized by the tumour cells, followed by breaking from the endosomes for the following intercellular applications.

After breaking from the endosomes, the five modules of nanorobots were toehold disintegrated to initiate the subsequent dual diagnosis. As illustrated in Scheme 1-b, eleven bases of 5' and 3'-termini on D1 and D2 were complementary to 22-nt targets of miR-21 and miR-224, respectively. Then, in CEM cells with high expression of miR-21 and miR-224, phi29 DNA polymerase-catalysed dual-RCA was triggered along with toehold disintegration (Scheme 1-c). Simultaneously, the ssDNA nanorobots were autonomously disintegrated into the five modules (closed D1, closed D2, S1, S2 and phi 29) for miRNA detection (Scheme 1-d) and drug release (Scheme 1-e). Subsequently, RCA products triggered by miR-21 and miR-224 hybridized with the FAM probe and Cy5 probe, respectively, to visualize the dual diagnosis (Scheme 1-f). Compared to the single RCA, this dual detection could also accelerate the disintegration of the nanorobots for more efficient detections²⁴. Concomitantly, two released modules, S1 and S2, contributed to subsequent tumour angiogenesis inhibition via synergistic silencing of VEGF²⁵ (Scheme 1-g). Overall, a ssDNA modular nanorobot was designed for targeted 'locked-open' dual recognition, toehold disintegration, dual diagnosis, precise siRNA delivery and synergistic gene therapy *in vivo*.

Characterizations of the ssDNA modular nanorobot and the feasibility for amplifications.

Morphological characterization of the ssDNA modular nanorobot was conducted by cryo-transmission electron microscopy (cryo-TEM) in aqueous buffer. Fig. 2a demonstrates the three upper edges of the tetrahedral structures, which exhibited an average diameter of approximately 50 nm for the ssDNA modular nanorobots. This size guaranteed the feasibility of the following *in vivo* delivery^{26,27}. As demonstrated by agarose gel electrophoresis, ssDNA modular nanorobots (Lane 4, Fig. 2b) migrated much slower than the modules of oligonucleotides D1, D2, S1 and S2. This indirectly confirmed the successful self-assembly of the five modules to form ssDNA modular nanorobots. Meanwhile, the low

mobility of the RCA product was recorded, which preliminarily confirmed the successful employment of RCAs after tetrahedral structure disintegration (Lane 5, Fig. 2b).

To further confirm the dissociation of the ssDNA modular nanorobot along with dual-RCA detection, D1 and D2 were modified by FAM and BHQ1 (black hole quencher 1), respectively. As designed (black line, Fig. 2c), the FAM signal was quenched in the modified hybridized duplex system of D1-D2. FL emission of FAM increased with the addition of the miR-21 or miR-224 target. This recovery of FAM signals confirmed the dissociation of the tetrahedral structure by RCA (blue and purple lines, Fig. 2c). It should be noted that the FL response was highest when both miR-21 and miR-224 were added simultaneously (red line, Fig. 2c). This was generated from synergistic RCA reactions devoted to faster and more efficient robot disintegrations. Therefore, the ssDNA modular nanorobot was successfully designed and could efficiently disintegrate into modules combined with intracellular target-triggered dual-RCA reactions.

To ensure the possibility of RCA-based dual detection, the enzyme-DNA conjugates in the enzyme loading module (Module III) were further evaluated. As designed, phi29 DNA polymerase was conjugated to thiolated poly-A^{28,29}. This would therefore hybridize with the poly-T stands in Module III to achieve enzyme modification. As shown in Fig. 2d, UV-vis absorption at 260 nm and 280 nm demonstrated the successful modification of the enzymes on the ssDNA modular nanorobots. In addition, the characteristic peaks of the phi29 polymerase in the circular dichroism (CD) spectrum also confirmed the enzyme modifications (Fig. 2e). Subsequently, whole ssDNA modular nanorobots were applied to RCA-based detection of miR-21 and miR-224 *in vitro*. Significant emissions at 520 nm (Fig. 2f) and 664 nm (Fig. 2g) were recorded and used for the detection of miR-21 and miR-224, respectively. The approximate exponential growth in the signals of miR-21 and miR-224 demonstrated the feasibility and potential of sensitive miRNA detection in a single cell.

Internalization and release of ssDNA modular nanorobots from endosomes

To visualize the release of ssDNA modular nanorobots from endosomes, Cy3-labelled S1 was prepared to fabricate Cy3-labelled nanorobots and incubated with CEM cells for imaging. Simultaneously, costaining of lysosomes and cell nuclei was performed with LysoTracker Green and 4',6-diamidino-2-phenylindole (DAPI), respectively. As demonstrated in Fig. 3a, after the first incubation of 2 h, the nanorobots were localized to lysosomes, as demonstrated by the overlapping red (Cy3-labelled nanorobots) and green (lysosomes) signals. This indicated the successful cellular internalization of ssDNA modular nanorobots through endocytosis during early incubation. After 6 h, we obtained dramatically increased red emissions together with unchanged green emission, which merged into an orange colour (Fig. 3a-6h). This pattern was generated from the successful entry of the ssDNA modular nanorobots into the cytoplasm by efficient endosomal escape or lysosome breaking^{30,31}.

The advantages of the rigid structure for *in vivo* applications were further examined. In the experiment, a Cy3-labelled negative control siRNA1 (NCsiRNA1) was prepared, whose overhanging 3' and 5' ends did not bind to D1 and D2. Then, with NCsiRNA1, a ssDNA system without rigid nanostructures (Cy3-labelled

ssDNA NC) was constructed for imaging. As shown in Fig. 3b, we obtained poor imaging with this controlled Cy3-labelled ssDNA NC system. This demonstrated the important role of rigid structures with tetrahedral tips in this internalization process. Therefore, rigid and stable ssDNA modular nanorobots were active for endocytic internalization, which could subsequently release modules from endolysosomes into the cytoplasm.

Logic dual recognition, delivery and cell imaging in living cells

Furthermore, the logic dual recognition of tumour cell membrane proteins for the selective delivery of bioreagents was examined. ssDNA modular nanorobots loaded with Cy3-labelled S1 (Cy3-labelled nanorobots) were selected as models for the experiments. As designed, under the guidance of two aptamers of sgc8c and scg4f, the ssDNA modular nanorobots targeted the corresponding receptors on the surfaces of tumour cells to form two G-quadruplexes. Subsequently, the Cy3-labelled nanorobots were selectively internalized by the tumour cells, which could be tracked by their Cy3 signals. To examine the logic dual recognition of tumour cells, four subtypes of cells (HeLa, Ramos, K562 and CEM cells) were imaged after incubation with Cy3-labelled nanorobots. The four cell lines have different patterns of expression of receptors of sgc8c and scg4f on their cell surfaces (Fig. 4b). As shown in Fig. 4a, we only observed significant red FL signals from CEM cells, which is the only one of the cell lines to express both receptors on its cell surface to allow for logic dual recognition. Quite low responses for HeLa cells and Ramos cells were recorded, with only one receptor highly expressed on each cell line. In addition, no obvious response was observed in K562 cells, which express neither of the two receptors on their cell surface. The corresponding comparison of Cy3 FL responses is shown in Figure 4b.

The logic dual recognition of the four cell lines is illustrated in Fig. 4c. As illustrated, the ON signal (Output 1) is output only if both receptors are highly expressed on the cell surface (e.g., CCRF-CEM cells). Conversely, OFF signalling (Output 0) is output in the absence of one (e.g., Ramos cells or HeLa cells) or both receptors (e.g., K562 cells)³². Therefore, we only observed significant Cy3 signals from CEM cells and in mixtures of HeLa and CEM cells (Output 1, Figure 4b). Nevertheless, quite low FL signals were observed from mixtures of HeLa and Ramos cells (Output 0, Figure 4b). This further confirmed the logic dual recognition of tumour cells, which could resist possible off-target deliveries from activated nanorobot diffusion or other physical contacts. Therefore, the logical dual recognition of tumour cells and the selective delivery of siRNA into tumour cells were confirmed.

Subsequently, after the logic dual-recognition and selective delivery of reagents into cells, the expression of biomarkers of miR-21 and miR-224 can also be imaged in cells. Herein, models with decreased expression of miR-21 and miR-224 in living CEM cells were constructed by adding target inhibitors to the cells. As shown in Fig. 4d, e, after incubation with ssDNA modular nanorobots, significant red (Cy5 for miR-21) and green (FAM for miR-224) signals were observed with obvious cytosolic localization in CEM cells. With miRNA inhibitor treatment, two remarkably decreased signals were recorded, in accordance with the downregulation of the miRNAs in the treated cells. This was also confirmed by traditional RT-PCR of cell extracts (Fig. 4f, g), which showed different miRNA expression levels for different cell lines.

Therefore, the reliability of applying the ssDNA modular nanorobots for miRNA knockdown has been confirmed in living cells.

Synergistic gene silencing and in vivo treatment

As reported recently, synergistic silencing of HER2 and VEGF can lead to significant cell morphology changes and substantial suppression of migration, spreading, cell adhesion, and proliferation^{31,32}. Furthermore, two small interfering RNAs (siRNAs) targeting VEGF (S1) and HER2 (S2) were reported to be feasible for synergistic silencing of VEGF. Therefore, the two siRNAs were selected for the experiments on synergistic gene silencing. To examine the synergistic gene silencing process, the ssDNA modular nanorobots were incubated with CEM cells (with high expression of VEGF) for 48 h. Guided by the sgc4f and sgc8c aptamer modules, the nanorobots entered the CEM cells under logic dual recognition. Then, VEGF mRNA and VEGF protein expression in cells with different treatments was evaluated by RT-PCR and enzyme-linked immunosorbent assay (ELISA). Fig. 5a, b demonstrates that no significant inhibition of VEGF mRNA or protein occurred when CEM cells were treated with no siRNA-loaded nanorobots, NCsiRNA2 (ineffective silencing)-loaded nanorobots, or a mixture of S1-S2. As expected, some inhibitory effects were exhibited after incubation with single siRNA-loaded nanorobots. Excitingly, we obtained the most significant inhibition of VEGF mRNA and proteins by treatment with the present ssDNA modular nanorobots. The level of suppression was comparable to the control transfection method via S1- and S2-loaded Lipo2000.

Finally, synergistic gene silencing by the present ssDNA modular nanorobots was evaluated in sorted CEM tumour-bearing nude mice. For better examinations, different groups of siRNA-loaded carriers were prepared to be delivered for gene silencing treatments. The drugs included no siRNA-loaded nanorobots, NCsiRNA2-loaded nanorobots, S1-loaded nanorobots, S2-loaded nanorobots, the present nanorobots, and S1- and S2-loaded Lipo2000. For *in vivo* examinations, the mice were treated with different siRNA-loaded carriers through tail vein injections. The tumour tissue sections were washed and stained with FITC-conjugated VEGF secondary antibody, and the nuclei were counterstained with DAPI. As demonstrated by immunofluorescence staining of tumour tissues (Fig. 5c), we obtained significantly decreased VEGF protein signals after treatment with the present ssDNA modular nanorobots. This confirmed the ideal treatment to obtain low expression of VEGF, which was comparable to the level of suppression after transfection by S1+S2 loaded Lipo2000. However, no significantly decreased expression was observed in the other groups, including no siRNA-loaded nanorobots, NCsiRNA2-loaded nanorobots or single siRNA-loaded nanorobots. Therefore, the synergistic therapy strategy of gene silencing has been confirmed, which overcame drug resistance by a single siRNA. It should be noted that as an emerging therapy technique, synergistic therapy is still in the early stages of exploration. The present work has confirmed and encouraged further developments in synergistic gene silencing therapy.

Meanwhile, to better examine S1 and S2 via *in vivo* visualization, S1 and S2 were labelled with Cy5 to evaluate the delivery and effective survival time of siRNA in tumour tissues. By ssDNA modular nanorobots, Cy5-labelled S1 and S2 were efficiently and specifically delivered into tumours and they even

maintained strong FL signals after 24 h (Fig. 5d). In fact, some nanorobots were also observed in the liver (Fig. 5e) during their detoxification process. Without the nanorobots, the delivery efficiency of free Cy5-siRNA was quite low, showing only weak FL signals in tumours that dramatically decreased over 24 h. Therefore, the tetrahedral structure played an effective role in special drug delivery and *in vivo* antidegradation.

Subsequently, via the successful delivery of ssDNA modular nanorobots, obvious suppression of the tumour was observed in the first three days (Fig. 5f). Fig. 5g shows the images of mice with obvious tumour suppression, which exhibited gradually decreased tumour sizes from 237 mm³ to 40 mm³ by the 17th day. Conversely, without the delivery of the nanorobots, the tumour size dramatically increased to 903 mm³ by the 17th day, similar to the blank control group treated with saline. As calculated, a 95.6% cure rate was obtained in 17 days. Furthermore, demonstrated by the H&E staining of tissue sections (Fig. 5h), we only observed significant cell apoptosis in tumour sections. Therefore, the present ssDNA modular nanorobots exhibited ideal treatment by synergistic gene silencing, which was demonstrated to be specific, efficient and safe.

Conclusion

In summary, guided by MD simulations in all-atom modelling of the dynamic folding process, a ssDNA modular nanorobot with multiple modules was successfully designed, optimized and prepared. This new design methodology broke through difficulties in designing ssDNA nanostructures and endowed modular nanorobots with high assembly efficiency. As calculated, the tetrahedral ssDNA modular nanorobot was stable, flexible, efficient, and had a low folding error for *in vivo* applications. Better than the 'side-by-side' manner of rigid dsDNA nanostructures, ssDNA modular nanorobots are more flexible for easy assembly of multiple modules and for subsequent flexible multiapplications. Therefore, with five functional modules, cancer special logic recognition and internalization, simple toehold disintegration, sensitive and selective dual diagnosis and visualization, and synergistic gene silencing treatments were successfully achieved. With multiple functions, such as logic internalization, good biocompatibility, accurate dual diagnosis and synergistic gene silencing, this computationally designed strategy has widened the bioapplications of DNA nanostructures in a smart way.

Declarations

Competing Interests statement

There are no competing interests to declare.

References

1. Li, S. P. et al. A DNA nanorobot functions as a cancer therapeutic in response to a molecular trigger *in vivo*. *Nat Biotechnol.* **36**, 258–264 (2018).

2. Hu, Y. et al. Dynamic DNA assemblies in biomedical applications. *Adv. Sci.* **7**, 2000557 (2020).
3. Rothemund, P. W. K. Folding DNA to create nanoscale shapes and patterns. *Nature* **440**, 297–302 (2006).
4. Li, J., Green, A. A., Yan, H. & Fan, C. H. Engineering nucleic acid structures for programmable molecular circuitry and intracellular biocomputation. *Nat. Chem.* **9**, 1056–1067 (2017).
5. Zhang, H. L. et al. DNA origami-based shape IDs for single-molecule nanomechanical genotyping. *Nat. Commun.* **8**, 14738 (2017).
6. Ke, Y. et al. Scaffolded DNA origami of a DNA tetrahedron molecular container. *Nano Lett.* **9**, 2445–2447 (2009).
7. Yao, G. B. et al. Programming nanoparticle valence bonds with single-stranded DNA encoders. *Nat Mater.* **19**, 781–788 (2020).
8. Jones, M. R. et al. DNA-nanoparticle superlattices formed from anisotropic building blocks. *Nat. Mater.* **9**, 913–917 (2010).
9. Douglas, S. M. et al. Rapid prototyping of 3D DNA-origami shapes with caDNAno. *Nucleic Acids Res.* **37**, 5001–5006 (2009).
10. Kim, D. N., Kilchherr, F., Dietz, H. & Bathe, M. Quantitative prediction of 3D solution shape and flexibility of nucleic acid nanostructures. *Nucleic Acids Res.* **40**, 2862–2868 (2012).
11. Yoo, J. & Aksimentiev, A. In situ structure and dynamics of DNA origami determined through molecular dynamics simulations. *Proc. Natl. Acad. Sci. U S A* **110**, 20099-20104 (2013).
12. Huang, C. M., Kucinic, A., Johnson, J. A., Su, H. J. & Castro, C. E. Integrated computer-aided engineering and design for DNA assemblies. *Nat Mater.* **20**, 1264–1271 (2021).
13. Watson, J. D. & Crick, F. H. C. Molecular structure of nucleic acids; a structure for deoxyribose nucleic acid. *Nature* **171**, 737–738 (1953).
14. Rosen, C. B. et al. Template-directed covalent conjugation of DNA to native antibodies, transferrin and other metal-binding proteins. *Nat. Chem.* **6**, 804–809 (2014).
15. Schaffert, D. H. et al. Intracellular delivery of a planar DNA origami structure by the transferrin-receptor internalization pathway. *Small* **19**, 2634–2640 (2016).
16. Pegram, M. D. & Reese, D. M. Combined biological therapy of breast cancer using monoclonal antibodies directed against HER2/neu protein and vascular endothelial growth factor. *Semin Oncol.* **29**, 29–37 (2002).
17. Tai, W. Y. Development of drug conjugates for cancer therapy and evaluation of dual siRNA silencing effect on breast cancer growth and invasion. 116–147 (2012).
18. Case, D. A. et al. AMBER 14, University of California, San Francisco, 2014.
19. Langecker, M. et al. Synthetic lipid membrane channels formed by designed DNA nanostructures. *Science* **338**, 932–936 (2012).
20. Hernández-Ainsa, S. et al. DNA origami nanopores for controlling DNA translocation. *ACS Nano* **7**, 6024–6030 (2013).

21. Snodin, B. E. et al. Introducing improved structural properties and salt dependence into a coarse-grained model of DNA. *J. Chem. Phys.* **142**, 234901 (2015).
22. You, M. X., Zhu, G. Z., Chen, T., Donovan, M. J. & Tan, W. H. Programmable and multiparameter DNA-based logic platform for cancer recognition and targeted therapy. *J. Am. Chem. Soc.* **137**, 667–674 (2015).
23. Ren, K. et al. A DNA dual lock-and-key strategy for cell-subtype-specific siRNA delivery. *Nat. Commun.* **7**, 13580 (2016).
24. Soengas, M. S., Gutierrez, M. S. & Salas, M. *J. Mol. Biol.* **253**, 517–529 (1995).
25. Konecny, G. E. et al. Association between HER-2/neu and vascular endothelial growth factor expression predicts clinical outcome in primary breast cancer patients. *Clin Cancer Res* **10**, 1706–1716 (2004).
26. Petros, R. A. & DeSimone, J. M. Strategies in the design of nanoparticles for therapeutic applications. *Nat. Rev. Drug Discov.* **9**, 615–627 (2010).
27. Cho, H. S. et al. Design consideration for tumour-targeted nanoparticles. *Nat. Nanotech.* **5**, 42–47 (2010).
28. Li, S. et al. A DNA nanorobot functions as a cancer therapeutic in response to a molecular trigger *in vivo*. *Nat. Biotechnol.* **36**, 258–264 (2018).
29. Schaffert, D. H. et al. Intracellular delivery of a planar DNA origami structure by the transferrin-receptor internalization pathway. *Small* **12**, 2634–2640 (2016).
30. Shen, X. T., Wang, Y., Zhang, Y., Ouyang, J. & Na, N. Unique SiO₂ nanourchins enable amplification in living cells for in situ imaging of mRNAs. *Adv. Funct. Mater.* **28**, 1803286 (2018).
31. Shen, X. T. et al. Biodegradable nanosyringes for intracellular amplification-based dual-diagnosis and gene therapy in single living cells. *Chem. Sci.* **10**, 6113–6119 (2019).
32. You, M. et al. DNA “Nano-Claw”: Logic-based autonomous cancer targeting and therapy. *J. Am. Chem. Soc.* **136**, 1256–1259 (2014).

Scheme

Scheme 1 is available in the Supplemental Files section

Figures

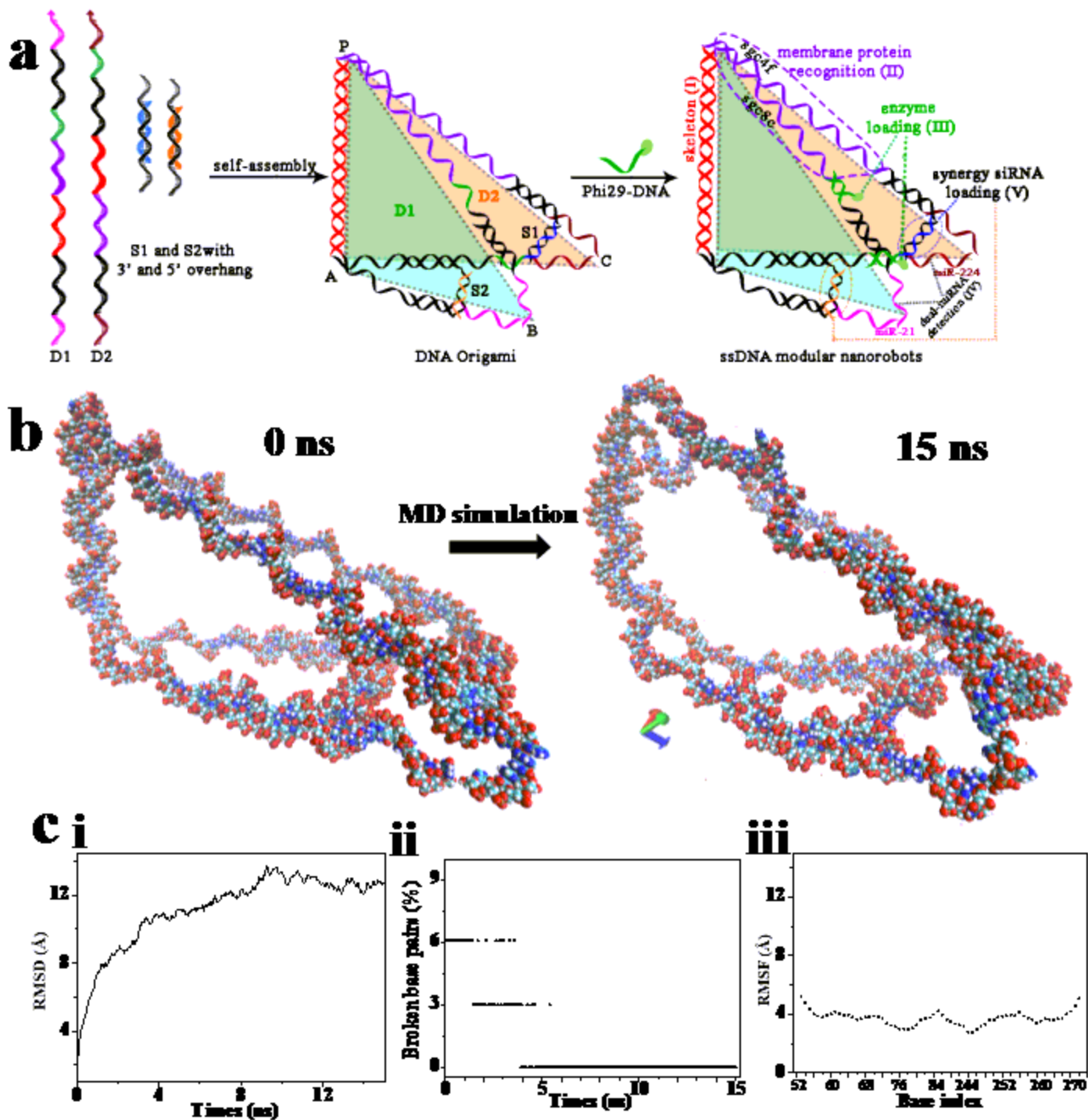


Figure 1

Design of ssDNA modular nanorobots. **a**, Illustration of the synthesis. The five modules include tetrahedron skeleton (I), logic cell membrane protein dual-recognition (II), enzyme loading (III), dual-targeted miRNA detection (IV) and synergy siRNA loading (V). **b**, All-atom MD simulations of the ssDNA modular nanorobot structures. The conformations of the tetrahedral structures at the beginning of the MD runs (0 ns, i) and at the end of the production MD runs (15 ns, ii). Mg²⁺ ions are shown as pink spheres. The systems contain 1,003,572 atoms (H₂O and Mg²⁺). **c**, All-atom MD simulations. (i) RMSD of

the DNA atoms from their initial coordinates during the MD simulations. (ii) The fraction of base pairs broken during the MD simulations. A base pair is considered to be broken when the distance between the N1 atom of the purine base and the N3 atom of the pyrimidine base exceeds 4 Å. The fraction of broken base pairs in the nanorobots versus the simulation time. (iii) RMSF of the dsDNA edges in the nanorobots. The values were computed using the coordinates of the base pair centres of mass and averaged over the last 10 ns of the corresponding MD trajectory.

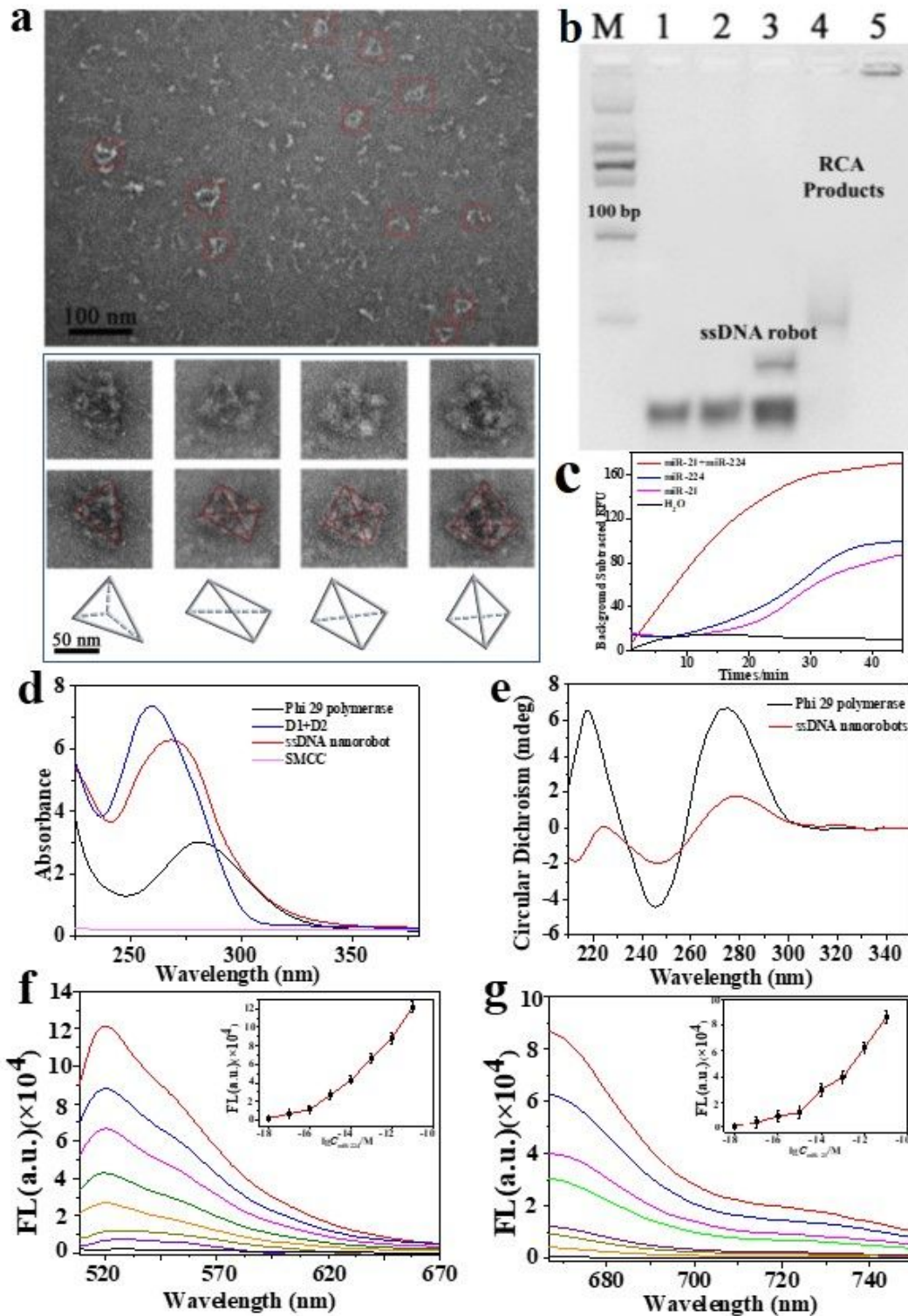


Figure 2

Morphological and chemical characterizations of ssDNA modular nanorobots. **a**, TEM images (top) and zoomed-in images (bottom) superimposed with the tetrahedron geometry. **b**, Agarose gel electrophoresis analysis. Lanes 1–5 represent D1, D2, D1+D2, ssDNA modular nanorobot and RCA products with two targets. **c**, FL spectra of duplex D1(FAM-modified)-D2(BHQ1-modified) with added targets. **d**, UV–vis absorption spectra. **e**, CD spectra of enzymes before and after conjugation. **f, g**, *In vitro* FL responses to different concentrations (1 aM to 100 pM) of miR-21 (520 nm) (**f**) and miR-224 (664 nm) (**g**). The insets: The relationship between FL responses and negative logarithmic values of miRNA concentrations (error bars show the mean standard deviation of three determinations).

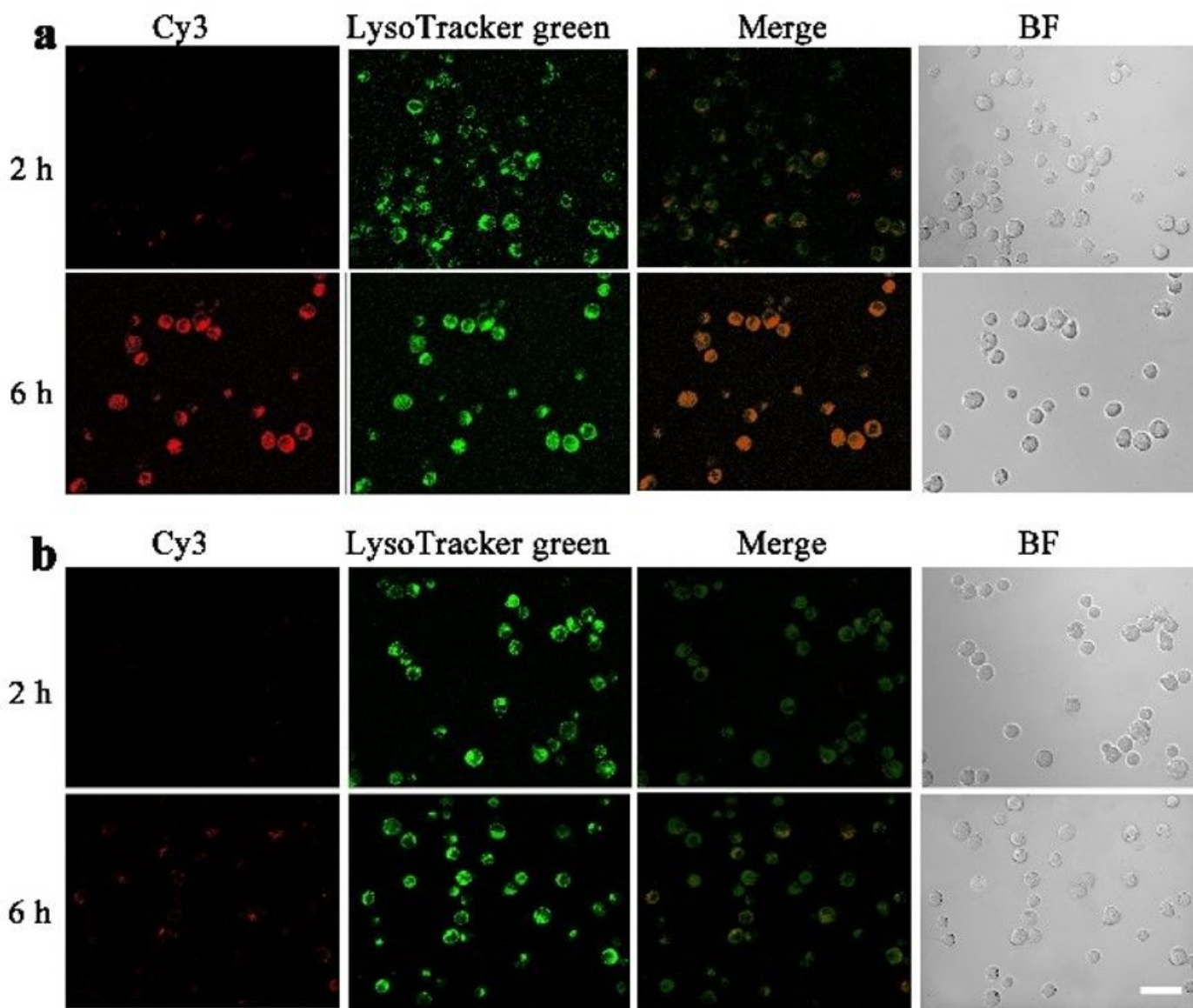


Figure 3

CEM cell imaging of ssDNA modular nanorobots. **a**, Costaining of CEM cells with LysoTracker Green and DAPI after incubation with Cy3-labelled nanorobots. **b**, Costaining of CEM cells with LysoTracker Green and DAPI after incubation with Cy3-labelled ssDNA NC. Scale bars: 10 μ m.

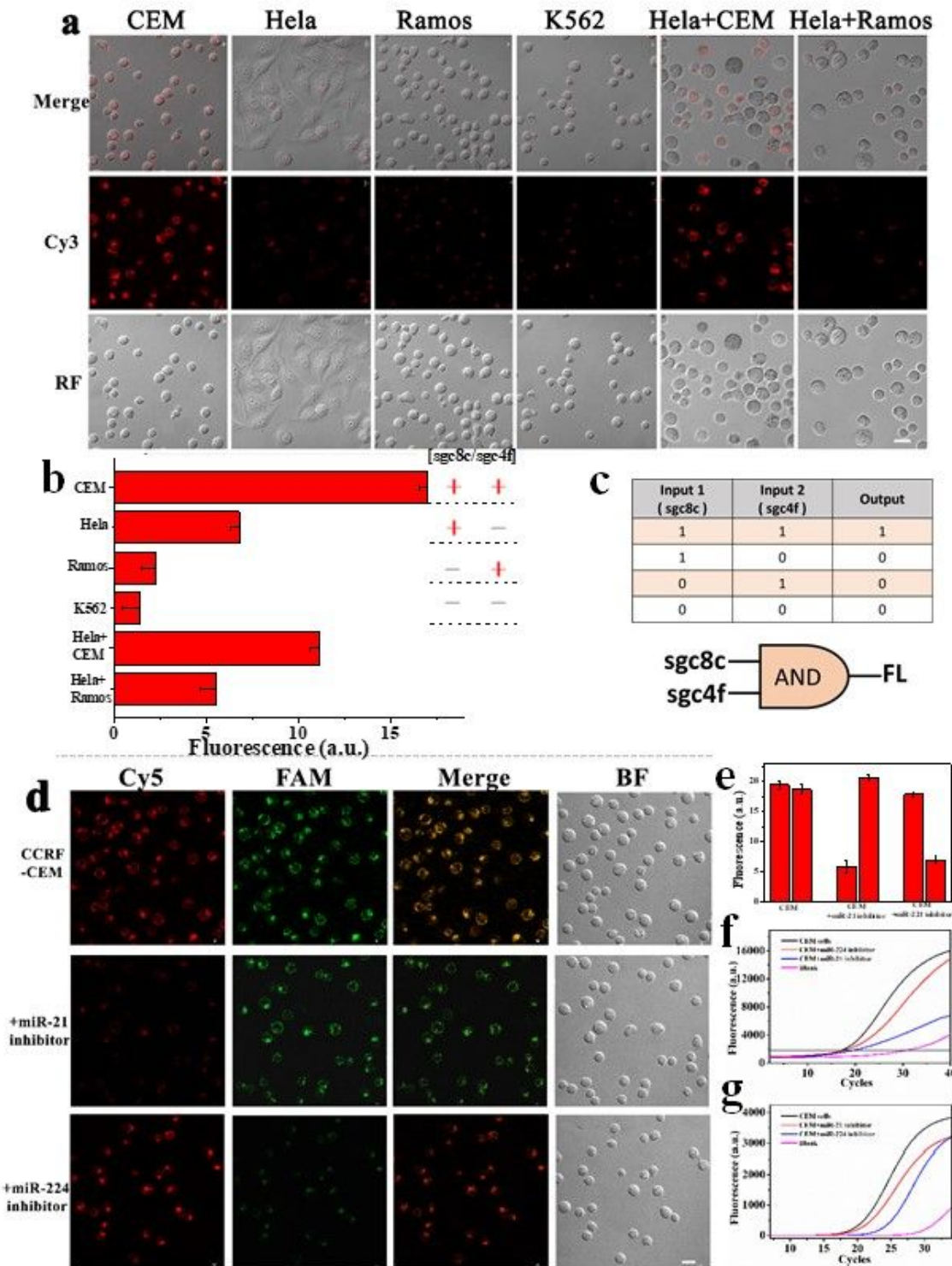


Figure 4

Cell imaging of miRNAs in CEM cells. **a**, Logic dual recognition and selective delivery of Cy3-labelled nanorobots (100 nM) into four cells lines and mixed cells. **b**, Corresponding FL signal comparison. Inset: the expression of acceptors of two aptamers (sgc8c and scg4f) on the cell surface. **c**, The potential logic gate system. **d**, Imaging after treatment with inhibitors of miR-21 or miR-224. **e**, Comparison of FL signals for *in vivo* imaging in Fig. 4d. **f, g**, RT-PCR detection of miR-21 (**f**) and miR-224 (**g**) from CEM cell extracts. Incubation for 6 h. Scale bars: 10 μ m.

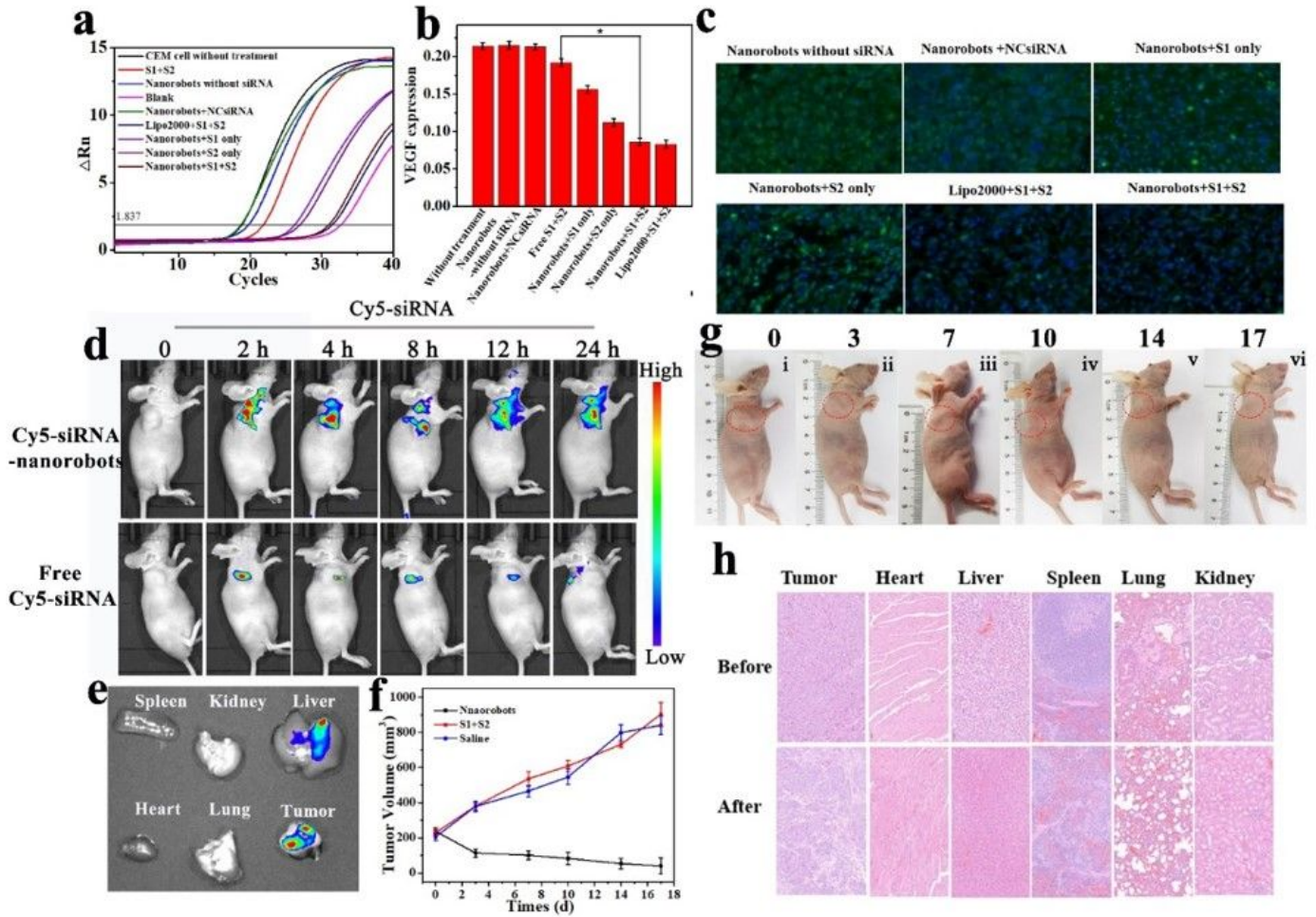


Figure 5

Gene silencing treatment of VEGF in CEM cells. **a**, RT-PCR for VEGF mRNA expression. **b**, ELISA for VEGF protein secretion levels. Groups: nanorobots without siRNA, NCsiRNA2-loaded nanorobots, S1+S2, only S1-loaded nanorobots, only S2-loaded nanorobots, present nanorobots, S1 and S2-loaded Lipo2000. The data and error bars indicate means \pm s.d. (n = 3). * $P < 0.05$ (two-tailed Student's t-test). Concentration: 100 nM. **c**, Immunofluorescence staining of tumour tissues from CEM tumour-bearing nude mice treated with different drug groups. **d**, *In vivo* optical imaging of mice injected with Cy5-labelled nanorobots and free Cy5-siRNAs (1.0 mg mL⁻¹ in PBS buffer). λ_{ex} : 640 nm. **e**, Ex vivo imaging of organs and tumour tissues. **f**, Size changes of tumours with time in different groups. **g**, Photographs of the tumour-bearing mice 0, 3, 7, 10, 14 and 17 days after injection. **h**, H&E staining images of tumours and other tissue sections.

Supplementary Files

This is a list of supplementary files associated with this preprint. Click to download.

- [Onlinefloatimage2.png](#)
- [SI.docx](#)